J Nanostruct 16(4): 4901-4912, Autumn 2026

RESEARCH PAPER

Fabrication of NiO/Fe_2O_3/PSi/p-Si nanocomposite Heterojunction for Application in Solar Cells

Ayat M. Jard *, *M. H. Al-Baghdadi*

Department of Physics, College of Education for Pure Sciences, University of Kerbala, Kerbala, Iraq

ARTICLE INFO

Article History:
Received 04 May 2026
Accepted 28 July 2026
Published 01 October 2026

Keywords:
Conversion solar cell efficiency
Heterojunction
Nanocomposite
Solar cell

ABSTRACT

In this work, Fe_2O_3 and NiO nanoparticles were used to prepare heterojunction solar cell. On other hand, PSi was prepared by using electrochemical etching technology. The Fe_2O_3 and NiO thin film samples were examined by X-ray diffraction (XRD), Atomic force microscopy (AFM), Field emission scanning electron microscopy (FE-SEM), Ultraviolet-visible (UV–Vis), Fourier transform infrared (FTIR) and PL emission. The Si wafer used in this work was p-type and had monocrystalline structure with direction (111) plane. it was a high peak emission near 640 nm was due to PSi nanocrystalline. The AFM test of porous silicon shows that the surface was like hills that were randomly, irregularly distributed, and had different heights, with RMS roughness (Sq): 2.37 nm, Mean roughness (Sa): 1.73 nm and Maximum height (Sz): 29.04. In other side, for Fe_2O_3 was agglomerated, semi-spherical nanoparticles and NiO NPs had spherical, porous, or nanosheet-like morphologies. The important binding group which informed Fe_2O_3 and NiO were specified by using FTIR spectrum. The energy band gap (direct and indirect) of Fe_2O_3-NPs was about 2.64 and 1.70 eV, respectively, and NiO-NPs was (3.62 eV). The efficiency of the produced solar cell was about 4.05%, and the filling factor 44.61%.

How to cite this article
Jard A., Al-Baghdadi M. Fabrication of NiO/Fe_2O_3/PSi/p-Si nanocomposite Heterojunction for Application in Solar Cells. J Nanostruct, 2026; 16(4):4901-4912. DOI: 10.22052/JNS.2026.04.036

INTRODUCTION

Nowadays, considerable attention has been attracted toward nanoparticles due to their special physical properties, which are different from those of bulk materials [1]. In previous decades, researchers have used metal oxide NP to implement a considerable number of developments in scientific applications. The applications of NP's could be in sensors, catalysts, medical sciences [2], batteries [3], capacitors and semiconductors. In the past years, iron oxide Fe_2O_3 is an n-type semiconductor in the hematite phase and has been attractive to many researchers' interests. It has many advantages, such as availability, low cost, non-toxicity, thermal stability and a narrow band gap energy near 2.2 eV [4, 5]. Fe_2O_3 has significant importance in solar cell applications, optoelectronics and energy conversion [6-11]. Fe_2O_3 nanoparticles can be formed by implementing many techniques, such as the chemical method [12], co-precipitation method [13], microwave-assisted synthesis [14], hydrothermal method [15], thermal decomposition [16], laser pyrolysis [17], and pulsed laser ablation [18, 19].

The heterojunction technique will largely

* *Corresponding Author Email: ayat.mosaa@s.uokerbala.edu.iq*

increase efficiency due to the lowering of energy loss by increasing the capture of sunlight [20-25], high performing, stability, high electrical production in both hot environmental and low sunlight conditions, and advantages over conventional solar cells. The (HJ) solar cells are used to limit the charge carrier flow or to collect them [26].

MATERIALS AND METHODS

Preparation of Fe_2O_3 and NiO materials

The material Nickel oxide (NiO) was prepared by using a chemical method. This molarity is recommended value for many researchers [27-29]. The nickel nitrate and sodium hydroxide serving as precursor materials to get 0.1 M. Initially, 2.9 g of nickel nitrate was dissolved in 100 mL deionized water, the previous solution was placed on a magnetic stirrer at 70 °C for one hour to ensure complete dissolution. Subsequently, a sodium hydroxide solution was prepared by dissolving 4 g of NaOH in 100 mL deionized water. The NaOH solution was then added dropwise to the nickel nitrate $Ni(NO_3)_2$ solution under continuous stirring with heating at 300 °C. A noticeable colour change was observed, indicating that the reaction and the formation of nickel oxide occurred. Approximately 20 mL of the sodium hydroxide solution was required to complete the reaction and until obtain a required NiO, colour then left the solution for 30 minutes.

NiO thin films were deposited on glass substrates using the same deposition conditions, utilizing a single concentration, while preserving identical spraying and drying parameters. The prepared samples were then used for structural, morphological, and optical tests before moving on to the cell-making stage.

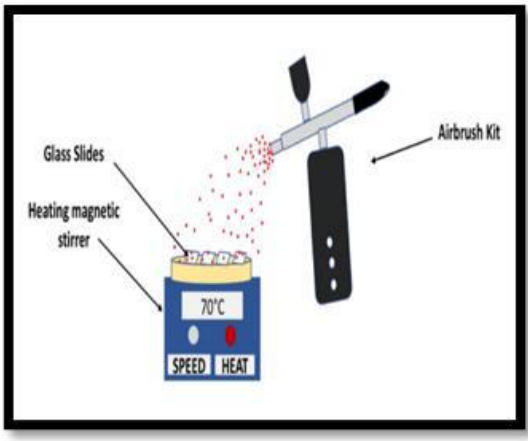

Fig. 1. The procedures used to manufacture NiO and Fe_2O_3 nanoparticles thin forms.

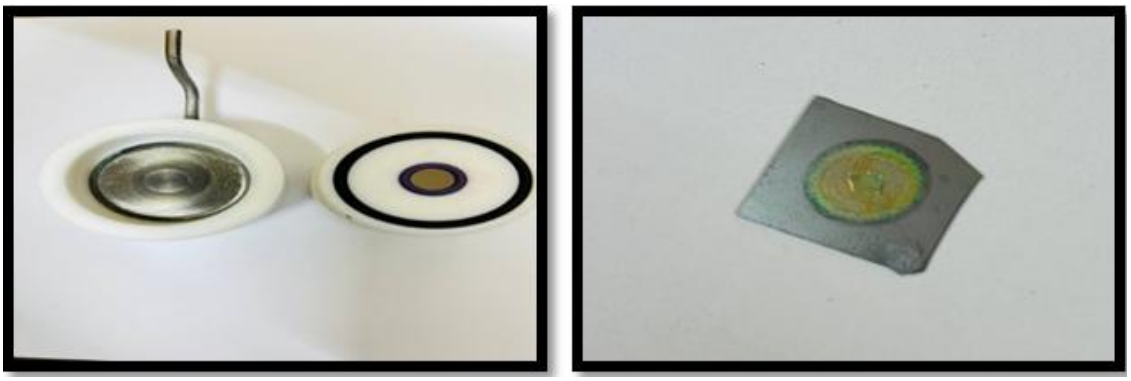

Fig. 2. a) the Teflon container, b) the silicon wafer after etching process.

All molar concentrations (0.05, 0.10, 0.15 and 0.20 M) have been used to deposit thin films of Fe_2O_3 on the glass substrates separately. The iron (III) oxide (Fe_2O_3) was dissolved with different molar concentrations by weighing appropriate amounts of Fe_2O_3 powder. Each concentration was dissolved separately in 100 mL of deionized water; the weight according to each concentration was (0.798, 1.59, 2.4 and 3.2 g), respectively, for each concentration. Before spraying, the Fe_2O_3 solution was heated to 70 °C to avoid inhomogeneity and to reduce the impact of thermal shock on the glass substrates. After that, the solution was put into a hand-held spray device (Airbrush Kit) as shown in Fig. 1. The deposition was done utilizing a manual spray deposition method, with a fixed spraying position and normal incidence angle at 90° toward the substrates. The solution was sprayed in successive bursts at a rate of four to five sprays per cycle, allowing the substrates to dry for a few minutes between each spraying cycle. The positions of the glass substrates were moved from time to time during the deposition process with tweezers to make sure that all samples were sprayed was in same conditions. Each glass substrate was exposed to approximately twenty spray cycles in total; this method gives an indication that all thin films prepared are approximately the same. The duration of deposition for each concentration was half an hour. Same way was followed for all Fe_2O_3 concentrations. After the deposition, the samples were left to dry at room temperature.

The density of the Fe2O3 and NiO are equal to (5.25, 6.67 g/cm3) respectively, the thin films thickness was approximately (0.9μm).

Preparation of Porous Silicon by Electrochemical Etching

The etching procedure starts after the washing of the silicon slides, where the silicon is immersed in a mixture of hydrofluoric acid (46%) and ethanol (99.99) in a 1:1 volume ratio (20 mL HF : 20 mL ethanol) at ambient temperature. The inclusion of ethanol serves to eliminate the Hydrogen bubbles formed on the surface, obstructing the process. The cell utilized in this method is constructed from Teflon, which is resistant to hydrofluoric acid. Teflon remains impervious to acid owing to its saturated condition and the presence of robust fluorine bonds.

where the silicon served as the positive electrode (anode), and gold was used as the negative electrode (cathode). The etching process was performed at a current density of 15 mA/cm² for a duration of 15 minutes. where the result after the etching process appeared to produce an etched area of the sample of almost (0.785) cm^2 as shown in Fig. 2.

Preparation Ag / NiO/ Fe_2O_3/ PS / Si / Ag SHJ solar cell

Thin films of Fe_2O_3 at different concentrations (0.05, 0.10 and 0.15 M) were utilized. A single-channel adjustable micropipette (10–100 µL) was used to drop Fe2O3 solution on PSi substrate. 50 µL amount of Fe_2O_3 solution was poured directly on PSi surface and left to deposit. Then the samples were put on a heated plate (70 °C) for about a minute to start drying and make sure the solvent evaporated equally over the whole PSi surface. The samples were gently tapped on the

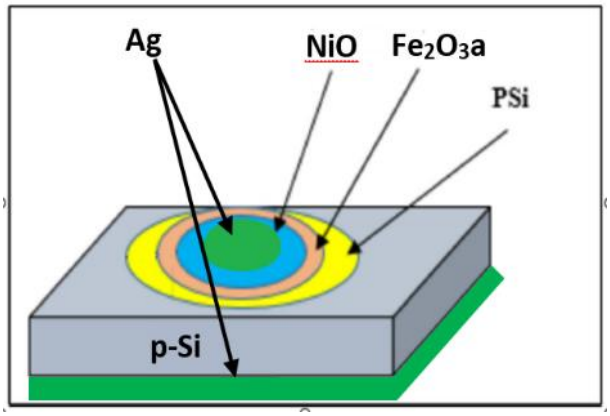

`Fig. 3. Schematic diagram of SHJ solar cell layers Ag/NiO/Fe_2O_3/PSi/Si/Ag.

heated plate to let trapped air bubbles out, make the thin film more homogeneous, and help the substance enter deeper into the porous silicon. This procedure helped prevent the formation of air bubbles and made it easy for Fe_2O_3 solution to enter the porous silicon structure.

Finally, the samples were put in an oven and heated to 100 °C for 1 hour to make sure the deposited layer stayed stable and stuck well to the substrate surface.

Nickel oxide (NiO) layer was added to each previous sample (using the same previous methodology). As shown in Fig. 3.

RESULTS AND DISCUSSION

Fig. 4 shows the crystalline structures of NiO and Fe_2O_3 with different concentration thin films, which were examined using X-ray diffraction (XRD) which has target (Cu-Kα) with wavelength (1.54060 Å). The XRD patterns of Fe_2O_3 thin film was taken

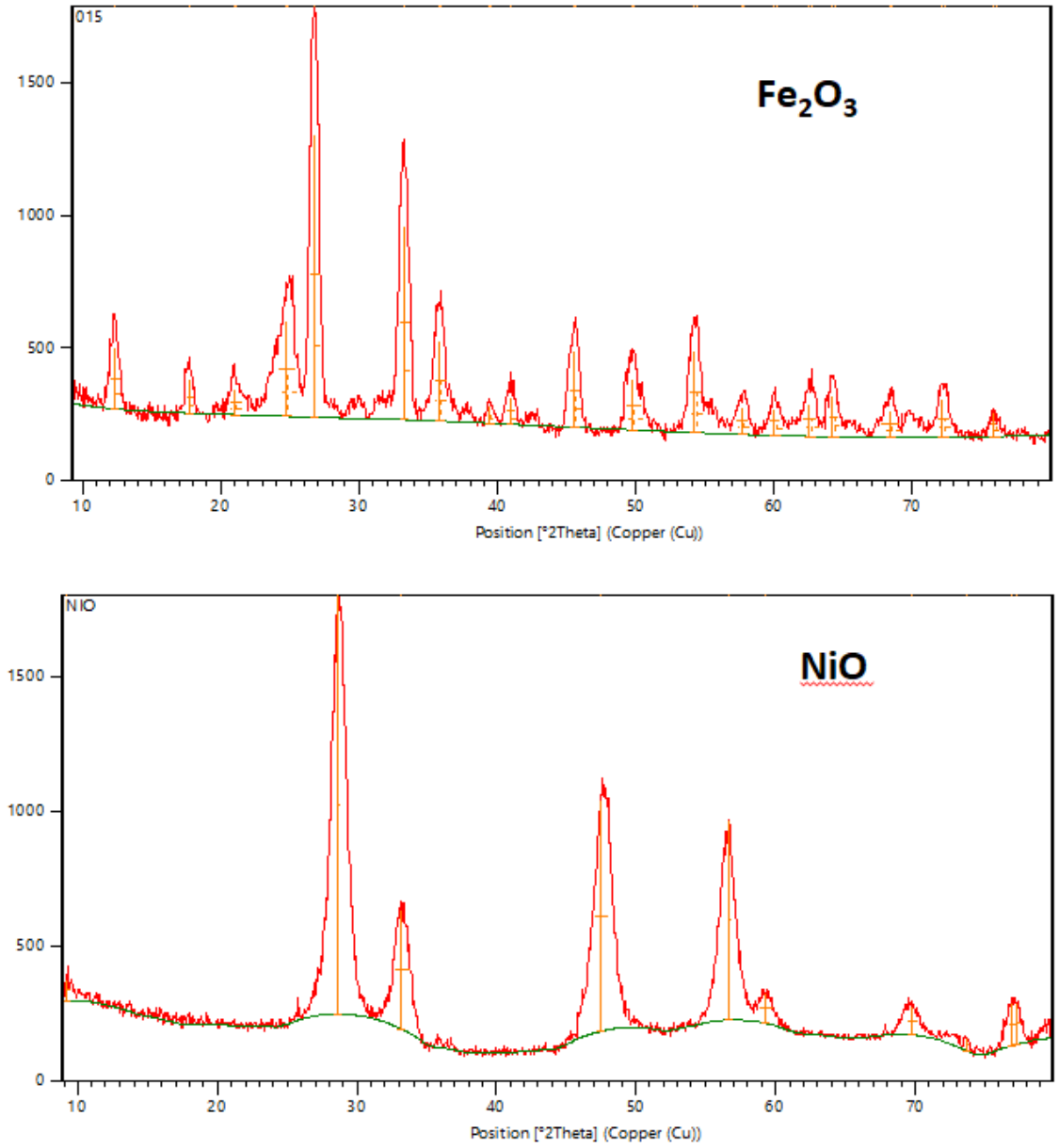

Fig. 4. XRD patterns of a) Fe_2O_3, b) NiO thin films.

by scanning 2θ between 9° and 80°. Fig. 4a shows the Fe2O3' s XRD pattern. The peaks were shown at angles of 26.6◦, 33.1◦, 35.7°, 40.8°, 49.7◦, 54.2◦, 57.6°, 62. 5◦, and 64.1◦, which matched to (012), (104), (110), (113), (024), (116), (018), (214) and (300) planes, respectively. The diffraction peaks of Fe_2O_3 are shown orthorhombic structures at dominant direction (104) for the highest intensity at 2θ = 33.099°. This result is in full agreement with [30-32], This pattern is aligned with the standard data from JCPDS card No. 01-1030 [30].

The XRD of NiO thin film shows the peaks at

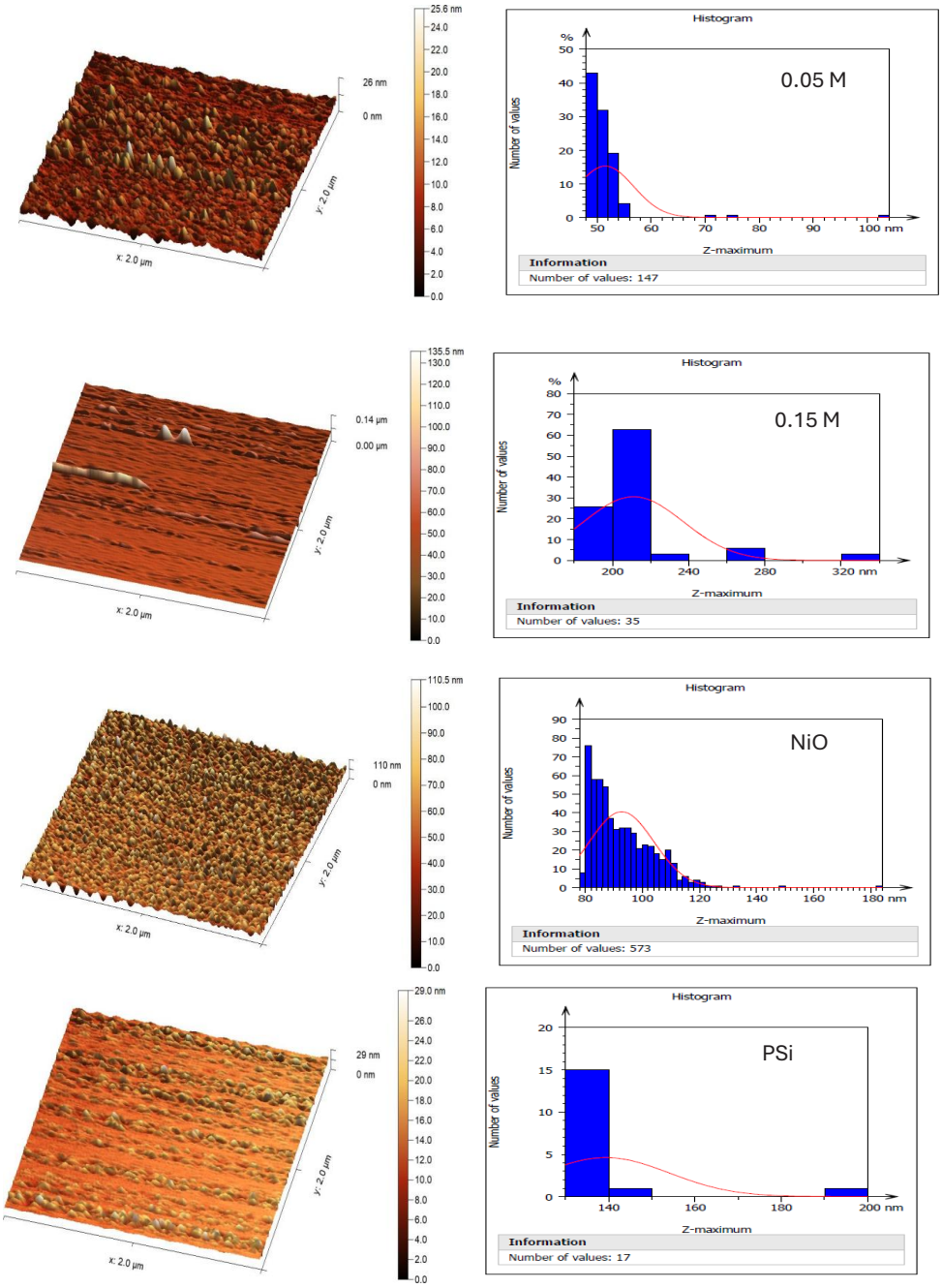

Fig. 5. Topography properties of: a) 0.15 M Fe_2O_3 b) 0.05 M Fe_2O_3 c) NiO d) PSi thin films by AFM.

2θ angles of 37.2◦, 43.3◦, 62.9°and 75.5°which points to (111), (200), (220) and (311) planes, respectively. NiO thin film refers to Face-Centered Cubic structures in the (200) direction for the highest intensity at 2θ = 47.4787°, This result is in full agreement with [33-34]. This pattern is aligned with the standard data from JCPDS card No. 04-0835 [35]. As shown in Fig. 4b.

The surface morphology was characterized by utilizing atomic force microscopy (Model TT-2 AFM workshop). as shown in Fig. 5. The AFM analysis in three dimensions for PSi, NiO and Fe_2O_3 with different concentration thin films, it shows an atomic force microscope with a scanning area of 2 µm. For PSi, and Fe_2O_3 there are irregular and randomly distributed hills and voids of nanocrystalline silicon throughout the whole surface. On other hand, for NiO there is more regularly hills distribution and fewer voids. This morphology of (Fe_2O_3 , Psi) increased the adhesion among layers. Tab. 1 explains some information related to the AFM test as shown in Table 1.

The emission spectra of PS with an etching current density of 15 mA/cm^2 at a constant period of 15 min and exposed to an excitation wavelength range from 320-900 nm is appeared in Fig. 6.

Because of porous silicon nanowires, the photoluminescence spectrum peak location and intensity are dependent on the quantum size effect, which appears in nanostructures. The highest amount of photoluminescence is due to the increasing porosity; otherwise, the blue shifting of the peak position is caused by a decreases in the silicon nanocrystalline size [36, 37].

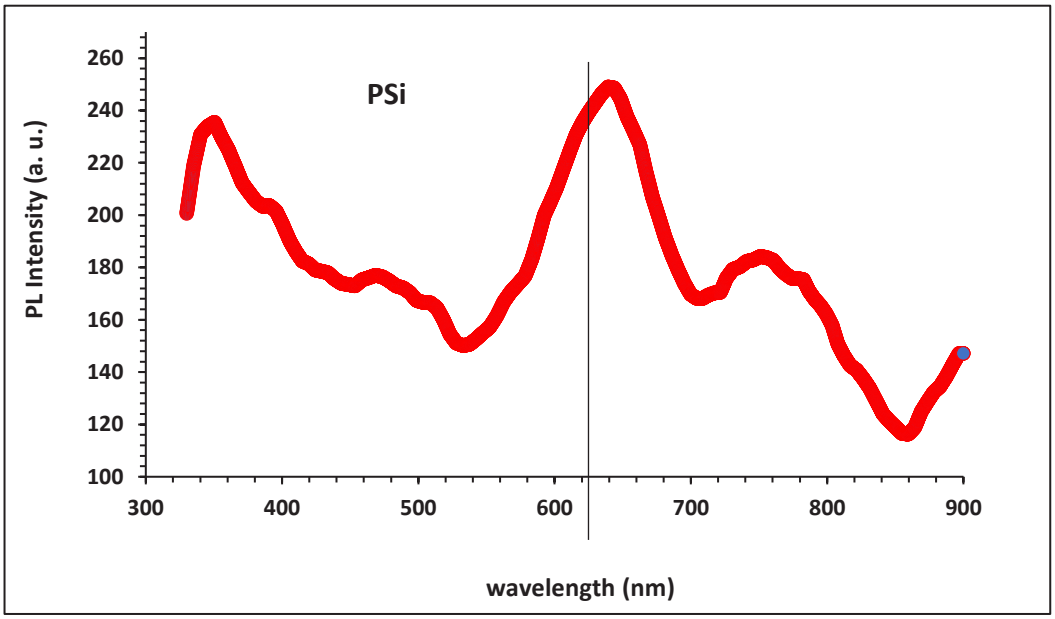

Fig. 6. The emission spectrum of PSi.

Table 1. AFM values of the maximum height (Sz), mean roughness (Sa) and RMS roughness (Sq) of Fe_2O_3, NiO and PSi.

Thin films	Molarity	Maximum height nm	Mean roughness nm	RMS roughness nm
Fe_2O_3	0.10	8.3331	1.97893	1.49183
	0.10	26.8956	4.89480	3.23650
	0.15	52.820	5.11461	3.08440
	0.20	126.192	21.5358	15.4617
NiO		129.9	11.51	14.58
PSi		29.04	1.73	2.37

In the FTIR spectrum, there are Resonances related to various wavenumbers that correspond to the absorption sites of the porous silicon, NiO and Fe_2O_3 thin films. An FTIR test of the porous silicon sample is shown in Fig. 7a. The peaks inside the FTIR spectra from 610 to 640 cm^{-1} are due to the bending vibration related to surface oxidation (Si-Si). The peaks from 800 to 880 cm^{-1} are due to the symmetric stretching which may indicate silicon oxide (Si-CH_3 or Si-O-S)). The peaks from 1050 to 1100 cm^{-1} are due to the asymmetric stretching vibration, which may indicate silicon oxide (Si-O-Si). The peaks from 1250 to 1270 cm^{-1} are due to the bending vibration, which confirms the presence of organic coverage (Si-CH_3). The peak from 1630 to 1640 cm^{-1} is due to the bending vibration, which confirms the water associated with the porous materials (H-O-H). The peaks

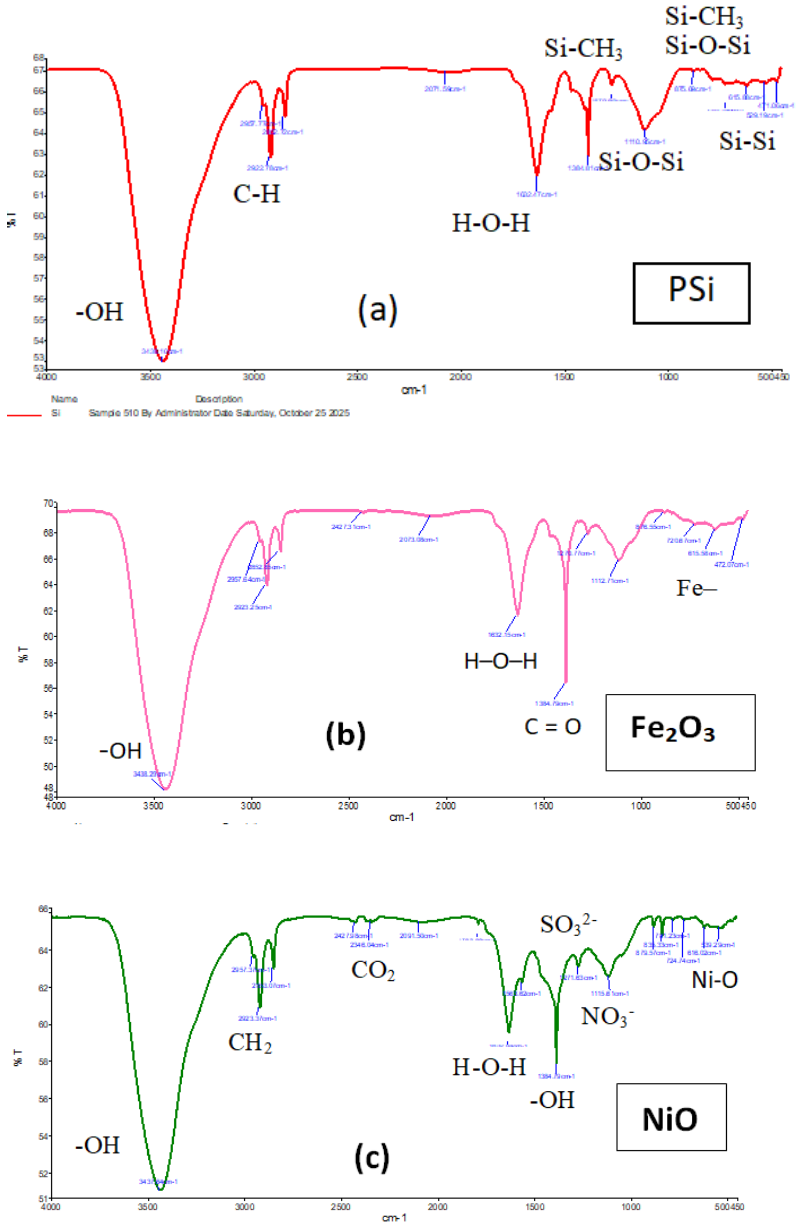

Fig. 7. FTIR analyses of Fe_2O_3, NiO and Psi thin films.

from 2900 to 3000 cm^{-1} are due to the stretching vibration, which indicates the presence of hydrocarbon groups (C-H). The peak from 3400 to 3600 cm^{-1} is due to the stretching vibration, which suggests moisture absorption (O-H). This result is in full agreement with [38-40].

The surface morphology image of the metal oxides Fe_2O_3 nanoparticles is shown in Fig. 7b; it shows the chemical bonds as well as the compound's functional groups. For the infrared spectrum (FTIR) for Fe_2O_3 nanoparticles at different molarities, the large and wide band at 3438cm^{-1} is related to the O-H stretching vibration for O-H groups. The absorption peaks near 1632cm^{-1} and 1384cm^{-1} are classified as the vibration of C=O, which are asymmetric and symmetric bending, and an absorption peak around 1270cm^{-1}. The band lower than 700 cm^{-1} is referred to Fe-O stretching mode. The band related to Fe-O stretching mode for Fe_2O_3 is shown at 576 cm^{-1}. This result is in full agreement with [33-35].

While, for NiO, which appeared many significant absorption peaks. It is shown in Fig. 7c, The peaks inside the FTIR spectra near 443.54 and 663cm^{-1} is due to the vibrations related to nickel oxygen bond stretching. The wide wideness of a peak gives an indicate that the NiO is crystalline in nature. 2346 cm^{-1} peak indicates the absorption band, which is due to the symmetric and asymmetric stretching modes related to the vibrations of the CO_2 molecule that is absorbed from the air [41]. Also, the broad absorption band centered at 3437, 1384 cm^{-1} is attributable to the band O–H stretching vibrations and the weak band near 1632 cm^{-1} is

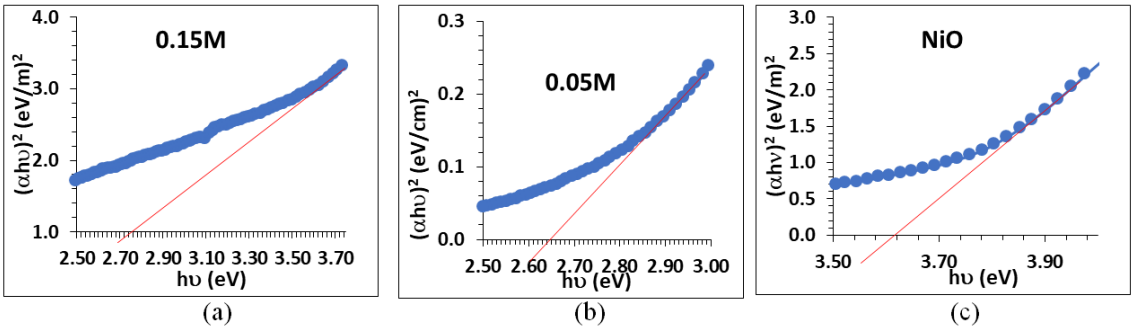

Fig. 8. Tauc's plot to get the direct and indirect for Fe_2O_3 energy gap and direct for NiO energy gap.

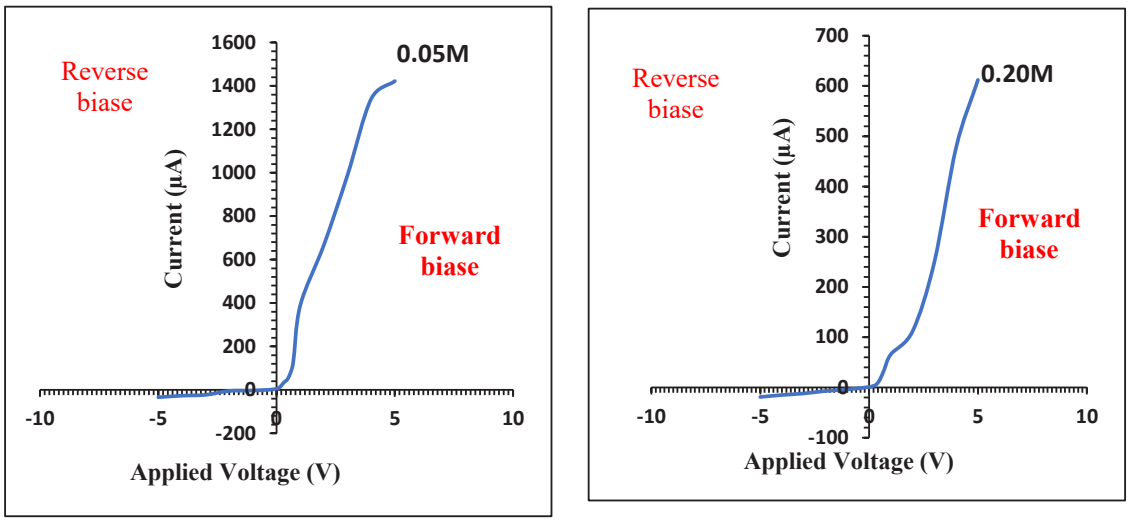

Fig. 9. The electrical measurements for Ag/ Fe_2O_3/NiO/Psi/p-Si/Ag solar cell at different Fe_2O_3 concentration.

assigned to H–O–H bending vibration mode. The bands at 1115 cm^{-1} are related to (C=O) group [42-45]. This result is in full agreement with [30-31].

The optical characteristics are crucial when studying solar cell efficiency. The direct and indirect band gap (Eg) can be obtained by linear fitting and extrapolating the line to the x-axis ($(\alpha h\nu)^2$ as a function of ($h\nu$)), as shown in Fig. 8a-b. The direct energy gap of Fe_2O_3 at different concentration is about 2.65, 2.70, 2.75 and 2.80 eV, respectively, with concentration. This result is fully agreement with references [36, 46-48].

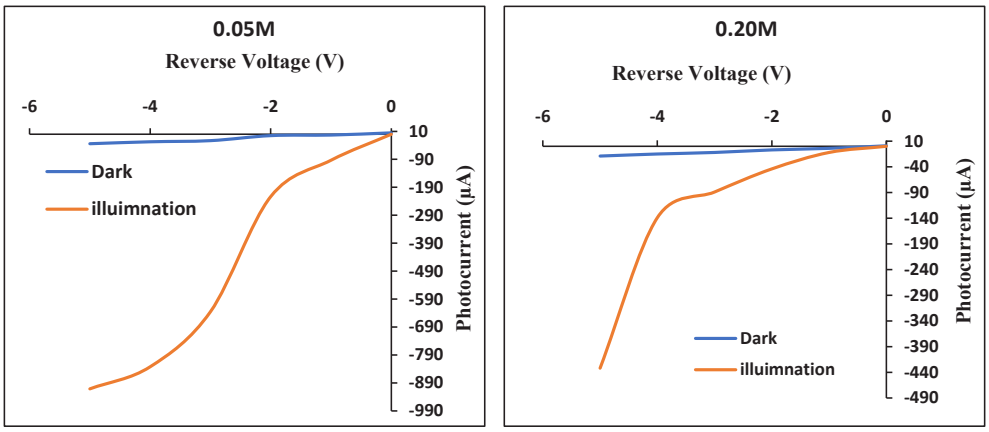

Fig. 10. I-V Characteristics for both case in dark and illuminated case when applied reverse bias of Ag/NiO/Fe_2O_3/Psi/Si/Ag solar cells at different Fe_2O_3 concentration.

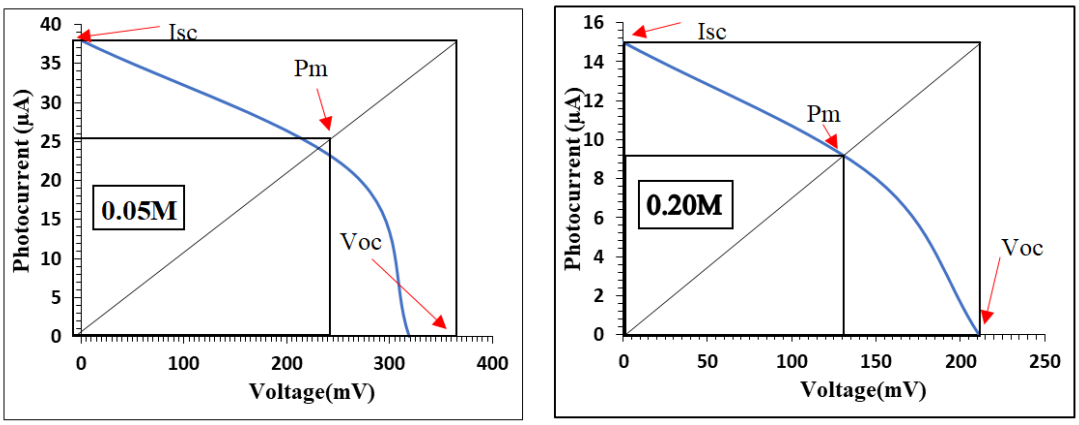

Fig. 11. The (I-V) characteristics of Ag/Nio/Fe_2O_3/PSi/Si/Ag SHJ at different Fe_2O_3 concentration.

Table 2. The values of (V_{oc}), (I_{sc}), (V_m), (I_m), (F.F%), and (η %) for manufactured SHJ solar cells.

SHJ solar cells	Fe_2O_3 Molarity	P_m µW	F.F %	η %
Ag/Nio/Fe_2O_3/PSi/Si/Ag	0.05M	5.41	62.8607	6.01
	0.10M	3.78	44.6190	4.05
	0.15M	1.47	30.5870	1.66
	0.20M	1.19	37.7883	1.30
Ag/Nio/PSi/Si/Ag		0.23	22.6190	0.26

While for NiO is about 3.62 eV as shown in Fig. 8 c. This result is fully agreement with references [33, 35]. As shown in Fig. 8 c.

The electrical measurement results related to the (I-V curve) for the Ag/NiO/Fe_2O_3/Psi/p-Si/Ag at different Fe_2O_3 concentration devices that were done under forward and reverse biasing in both dark and light conditions are shown in Fig. 9. The cell is tested under standard test conditions (STC), which specify a light intensity of 1000 W/m² (AM1. 5G spectrum) and a cell temperature of 25°C. These measurements are principally to describe the device's performance. The decreasing width of depletion region's as forward bias voltage increases. In contrast, the increasing width of depletion region's as reverse bias voltage, so there is no current flows.

When applied forward bias voltage, the majority charge carriers in both side of potential barrier are injected inside the depletion region, as a result, the width of depletion region was reduced and number of majority and minority carriers per unit volume in increased. In the case of illumination, a heterojunction was exposed to visible light which passed through NiO layer, but it absorbed by the Fe_2O_3 and PSi and Si substrate. This will lead to generate the e-h pairs near the NiO/Fe_2O_3/Psi/p-Si interface and increasing photocurrent with increasing bias voltage [49–51].

In Fig. 10, it is clear that the values of current in illuminated case is higher than dark case at reverse bias at different Fe_2O_3 concentration, so the current is independent on the applied voltage in this case, but it is due to the enhance in the absorption of incident photons because the increasing of reflections from the nanowire on the surface of porous silicon then give the Fe_2O_3 film more ability to absorb the photons.

The (I-V) characteristics of the solar cell Ag/ NiO/Fe_2O_3/Psi/p-Si /Ag at different Fe_2O_3 concentrations are shown in Fig. 11, which explains a schematic diagram for Ag/ NiO/Fe_2O_3/ Psi/p-Si /Ag solar cells. It displays that the open-circuit voltage (V_{OC}) was measured at I = 0, and the short-circuit current value (I_{SC}) was obtained at V = 0, as indicated in Table 2, where the fill factor (F.F.) as well as photovoltaic conversion solar cell efficiency (η) are calculated using the following formulas (Eqs. 1 and 2) [52]. The intensity of the Philips Halogen lamp (P_{in}) used for illumination was 100 mW/cm²:

$$\text{Fillin Factor} = \frac{\text{maximum power } (P_m)}{\text{maximum voltage } (V_m) \times \text{current maximum } (I_m)} \quad (1)$$

$$\text{Efficiency } (\eta) = \frac{I_m \times V_m}{\text{input intensity} \times \text{area}} \times 100\% \quad (2)$$

This result means that this synthesis of a heterojunction gets good performance related to Ag/NiO/Fe_2O_3/PSi/p-Si/Ag solar cells.

CONCLUSION

The characterization of precipitated Iron Oxide and Nickel oxide films was done by the drop casting method, which is a simple method; these films were deposited on glass substrates. The optical properties were examined using the UV-spectrum, and with using Taus equation, the electronic transmissions (direct and indirect transmissions) were defined with the presence of two different optical energy gaps; both locations were in the visible region.

Ag/NiO/Fe_2O_3/PSi/p-Si/Ag solar cells were manufactured using electrochemical etching of p-type silicon. NiO had good transparency in the spectral range (400-1100) nm. The electrical properties were dependent on the energy gap of nanomaterials. The result has been got in this work (F.F, η) are higher and better than reported papers.

CONFLICT OF INTEREST

The authors declare that there is no conflict of interests regarding the publication of this manuscript.

REFERENCES

1. Ramalingam S, Muralidharan VS, Subramania A. Electrodeposition and characterization of Cu-TiO_2 nanocomposite coatings. J Solid State Electrochem. 2009;13(11):1777-1783.
2. Dalla Pria P. Evolution and new application of the alumina ceramics in joint replacement. European Journal of Orthopaedic Surgery and Traumatology. 2007;17(3):253-256.
3. Dillon AC, Mahan AH, Deshpande R, Parilla PA, Jones KM, Lee SH. Metal oxide nano-particles for improved electrochromic and lithium-ion battery technologies. Thin Solid Films. 2008;516(5):794-797.
4. Al-Kuhaili MF, Saleem M, Durrani SMA. Optical properties of iron oxide (α-Fe_2O_3) thin films deposited by the reactive evaporation of iron. J Alloys Compd. 2012;521:178-182.
5. Sabry RS, Al-Haidarie YK, Kudhier MA. Synthesis and photocatalytic activity of TiO2 nanoparticles prepared by sol–gel method. J Sol-Gel Sci Technol. 2016;78(2):299-306.

6. Long NV, Teranishi T, Yang Y, Thi CM, Cao Y, Nogami M. Iron Oxide Nanoparticles for Next Generation Gas Sensors. International Journal of Metallurgical and Materials Engineering. 2015;1(2).
7. Shinde SS, Bansode RA, Bhosale CH, Rajpure KY. Physical properties of hematite α-Fe_2O_3 thin films: application to photoelectrochemical solar cells. Journal of Semiconductors. 2011;32(1):013001.
8. Wang C, Wang L, Tang K. Synthesis of Mesoporous Fe_2O_3 Nanorods and Their Electrochemical Performance. International Journal of Electrochemical Science. 2013;8(4):4543-4550.
9. Wang KX, Yu Z, Liu V, Brongersma ML, Jaramillo TF, Fan S. Nearly Total Solar Absorption in Ultrathin Nanostructured Iron Oxide for Efficient Photoelectrochemical Water Splitting. ACS Photonics. 2014;1(3):235-240.
10. Kumar Dalapati G, Masudy-Panah S, Kumar A, Cheh Tan C, Ru Tan H, Chi D. Aluminium alloyed iron-silicide/silicon solar cells: A simple approach for low cost environmental-friendly photovoltaic technology. Sci Rep. 2015;5(1).
11. Daothong S. Characterization of Fe_2O_3 Nanowires and its Solar Cell Applications. Key Eng Mater. 2018;766:217-222.
12. Mamani JB, Gamarra LF, Brito GEdS. Synthesis and characterization of Fe3O4 nanoparticles with perspectives in biomedical applications. Materials Research. 2014;17(3):542-549.
13. Hariani PL, Faizal M, Ridwan R, Marsi M, Setiabudidaya D. Synthesis and Properties of Fe3O4 Nanoparticles by Co-precipitation Method to Removal Procion Dye. International Journal of Environmental Science and Development. 2013:336-340.
14. Lastovina TA, Budnyk AP, Soldatov MA, Rusalev YV, Guda AA, Bogdan AS, et al. Microwave-assisted synthesis of magnetic iron oxide nanoparticles in oleylamine–oleic acid solutions. Mendeleev Commun. 2017;27(5):487-489.
15. Hayashi H, Hakuta Y. Hydrothermal Synthesis of Metal Oxide Nanoparticles in Supercritical Water. Materials. 2010;3(7):3794-3817.
16. Lassenberger A, Grünewald TA, van Oostrum PDJ, Rennhofer H, Amenitsch H, Zirbs R, et al. Monodisperse Iron Oxide Nanoparticles by Thermal Decomposition: Elucidating Particle Formation by Second-Resolved in Situ Small-Angle X-ray Scattering. Chem Mater. 2017;29(10):4511-4522.
17. Alexandrescu R, Bello V, Bouzas V, Costo R, Dumitrache F, García MA, et al. Iron Oxide Materials Produced by Laser Pyrolysis. AIP Conference Proceedings: AIP; 2010. p. 22-25.
18. Hameed MM, Al-Samarai A-ME, Aadim KA. Synthesis and Characterization of Gallium Oxide Nanoparticles using Pulsed Laser Deposition. Iraqi Journal of Science. 2020:2582-2589.
19. Khashan KS, Sulaiman GM, Mahdi R. Preparation of iron oxide nanoparticles-decorated carbon nanotube using laser ablation in liquid and their antimicrobial activity. Artificial Cells, Nanomedicine, and Biotechnology. 2017;45(8):1699-1709.
20. Shaw P. Eckardt, F. D. (ed.) (2022): Landscapes and Landforms of Botswana. Springer, Cham, Switzerland. xxiii, 403 p., 265 figures and tables. ISBN 978-3-030-86101-8. Zeitschrift für Geomorphologie. 2022;64(1):73-75.
21. Descoeudres A, Barraud L, De Wolf S, Strahm B, Lachenal D, Guérin C, et al. Improved amorphous/crystalline silicon interface passivation by hydrogen plasma treatment. Appl Phys Lett. 2011;99(12).
22. Olibet S, Vallat-Sauvain E, Ballif C. Model for a-Si:H/c-Si interface recombination based on the amphoteric nature of silicon dangling bonds. Physical Review B. 2007;76(3).
23. Taguchi M, Terakawa A, Maruyama E, Tanaka M. Obtaining a higherVoc in HIT cells. Progress in Photovoltaics: Research and Applications. 2005;13(6):481-488.
24. Zhang D, Tavakoliyaraki A, Wu Y, van Swaaij RACMM, Zeman M. Influence of ITO deposition and post annealing on HIT solar cell structures. Energy Procedia. 2011;8:207-213.
25. Wolf SD, Descoeudres A, Holman ZC, Ballif C. High-efficiency Silicon Heterojunction Solar Cells: A Review. green. 2012;0(0).
26. Gxasheka AR, van Dyk EE, Vorster FJ. Local photo-response measurements of photovoltaic devices. physica status solidi c. 2008;5(2):645-648.
27. Owoeye VA, Adewinbi SA, Salau AO, Orelusi AN, Adeoye AE, Akindadelo AT. Effect of precursor concentration on stoichiometry and optical properties of spray pyrolyzed nanostructured NiO thin films. Heliyon. 2023;9(1):e13023.
28. Ukoba OK, Eloka-Eboka AC, Inambao FL. Influence of concentration on properties of spray deposited nickel oxide films for solar cells. Energy Procedia. 2017;142:236-243.
29. Soylu M. Solution molarity dependent structural and optical properties of CdO nanostructured thin films. Optik. 2020;216:164865.
30. Chakraborty AR, Zohora Toma FT, Alam K, Yousuf SB, Hossain KS. RETRACTED: Influence of annealing temperature on Fe_2O_3 nanoparticles: Synthesis optimization and structural, optical, morphological, and magnetic properties characterization for advanced technological applications. Heliyon. 2024;10(21):e40000.
31. Sankadiya S, Oswal N, Jain P, Gupta N. Synthesis and characterization of Fe_2O_3 nanoparticles by simple precipitation method. AIP Conference Proceedings: American Institute of Physics; 2016. p. 020064.
32. Vuong DD, Hien VX, Trung KQ, Chien ND. Synthesis of SnO_2 micro-spheres, nano-rods and nano-flowers via simple hydrothermal route. Physica E: Low-dimensional Systems and Nanostructures. 2011;44(2):345-349.
33. Khairnar SD, Shrivastava VS. Facile synthesis of nickel oxide nanoparticles for the degradation of Methylene blue and Rhodamine B dye: a comparative study. Journal of Taibah University for Science. 2019;13(1):1108-1118.
34. Mohammed M, Al khazraji AH. Synthesis and Characterization of Nickel Oxide Nanoparticles by Green as well as Chemical Routes and Comparisons their Properties. Iraqi Journal of Natural Sciences and Nanotechnology. 2023;4:54-63.
35. Qiao H, Wei Z, Yang H, Zhu L, Yan X. Preparation and Characterization of NiO Nanoparticles by Anodic Arc Plasma Method. Journal of Nanomaterials. 2009;2009(1).
36. Latiff DMA, Ahmed BA, Ali SM, Jasim KA. Fabrication and characterization of Se66S44-xAsx thin films chalcogenide. Chalcogenide Letters. 2025;22(6):521-528.
37. Ali MY, Al-Azzawi MA, Abad WK, Abd AN. Vanadium Pentoxide and Bismuth Oxide Thin Films Deposition on PSi for Application in Solar Cells. Silicon. 2025;17(3):625-634.
38. Herynková K, Podkorytov E, Šlechta M, Cibulka O, Leitner J, Pelant I. Colloidal solutions of luminescent porous silicon

clusters with different cluster sizes. Nanoscale Research Letters. 2014;9(1).
39. Hadi Hussein H. Study of Characteristics of Porous Silicon by Electrochemical Etching. Engineering and Technology Journal. 2013;31(1B):34-38.
40. Mutlak FAH. Porous silicon prepared by photo electrochemical etching assisted by laser. Iraqi Journal of Physics. 2019;15(32):122-129.
41. Jayakumar G, Albert Irudayaraj A, Dhayal Raj A. Photocatalytic Degradation of Methylene Blue by Nickel Oxide Nanoparticles. Materials Today: Proceedings. 2017;4(11):11690-11695.
42. Kayani ZN, Butt M, Ali Y, Riaz S, Naseem S. Structural and Optical Study of NiO Nano-particles. Materials Today: Proceedings. 2015;2(10):5804-5807.
43. Vijaya Kumar P, Jafar Ahamed A, Karthikeyan M. Synthesis and characterization of NiO nanoparticles by chemical as well as green routes and their comparisons with respect to cytotoxic effect and toxicity studies in microbial and MCF-7 cancer cell models. SN Applied Sciences. 2019;1(9).
44. Rajith Kumar CR, Betageri VS, Nagaraju G, Pujar GH, Suma BP, Latha MS. Photocatalytic, nitrite sensing and antibacterial studies of facile bio-synthesized nickel oxide nanoparticles. Journal of Science: Advanced Materials and Devices. 2020;5(1):48-55.
45. Two-Dimensional Room-Temperature Magnetic Nonstoichiometric Fe7Se8 Nanocrystals: Controllable Synthesis and Magnetic Behavior. American Chemical Society (ACS).
46. Dadashi S, Poursalehi R, Delavari H. Structural and Optical Properties of Pure Iron and Iron Oxide Nanoparticles Prepared via Pulsed Nd:YAG Laser Ablation in Liquid. Procedia Materials Science. 2015;11:722-726.
47. S. Alnaily R, L. Sheqnab M. Study the optical and structure properties of CdTe nanoparticles prepared by pulsing laser ablation in distilled water. Journal of Kufa-Physics. 2019;11(1):82-89.
48. Nanoparticles of Metal Oxide (Bi_2O_3/PSi/n-Si) for Photovoltaic Applications. Nanosistemi, Nanomateriali, Nanotehnologii. 2024;22(2).
49. Salih AA, Abad WK, Fadaam SA, Hussein BH. Fabrication of lead oxide nanoparticles by green synthesis method for photovoltaic applications. Digest Journal of Nanomaterials and Biostructures. 2023;18(4):1225-1233.
50. Saeed SI, Ali MA, Abad WK, Abd AN. Low-Cost Applications by Simple Chemical Method: Solar Cell and Photodetector. International Journal of Nanoscience. 2023;23(02).
51. Sood S, Umar A, Kumar Mehta S, Kumar Kansal S. α-Bi_2O_3 nanorods: An efficient sunlight active photocatalyst for degradation of Rhodamine B and 2,4,6-trichlorophenol. Ceram Int. 2015;41(3):3355-3364.
52. Hameed Hussein A, Abduallah Mahmoud A, Ahmed Naji A. Biosynthesis and characterization of (Co_3O_4) for solar cell applications via N-Sativa extract. Global Journal of Engineering and Technology Advances. 2023;14(3):033-041.